

# A Passive PEEC-Based Micromodeling Circuit for High-Speed Interconnection Problems

Yuhang Dou, *Student Member, IEEE*, and Ke-Li Wu<sup>✉</sup>, *Fellow, IEEE*

**Abstract**—A passive partial element equivalent circuit (PEEC)-based micromodeling circuit is proposed for time-domain simulation of a high-speed interconnection problem. This physics-based model order reduction method derives a concise and physically meaningful circuit model from the PEEC model by absorbing its insignificant nodes. To maintain high fidelity of the original electromagnetic PEEC model, the concept of pseudoinductor is introduced to the node-absorbing process. The derivation process does not involve any matrix inversion or decomposition and is highly suitable for GPU parallel computations. Passivity of the micromodeling circuit is ensured by a new passivity checking and enforcement method proposed for the first time. As the scale of the micromodeling circuit can be one order of magnitude smaller than that of the original PEEC model, the time-domain simulation can be three orders of magnitude faster. Two practical examples are given to demonstrate the high fidelity, scalability, and accuracy of the proposed micromodeling circuit, showing excellent applicability to high-speed interconnection problems.

**Index Terms**—Electromagnetic (EM) modeling, equivalent circuit, model order reduction (MOR), partial element equivalent circuit (PEEC), signal integrity (SI).

## I. INTRODUCTION

**S**IGNAL integrity (SI) is a set of measures of the quality of an electrical signal. A digital signal with good SI must have stable and valid logic levels; accurate placement in time; clean and fast transitions; and be free of any transients [1]. Nowadays, it is increasingly critical to ensure a good SI design of interconnection and packaging circuits for high-speed digital signals [2] with the continuous increase of data rate and circuit density. Usually, eye diagram is used as a visual indicator to observe the general SI on a clocked bus, for which passivity of the model simulated in time-domain is required and simulation time must be bearable.

The partial element equivalent circuit (PEEC) model [3] converts a multiconductor electromagnetic (EM) problem into a circuit model, which can be solved by Modified Nodal Analysis (MNA) [4] or a SPICE-like solver. It has been widely adopted in SI analysis, electronic packaging design,

EM radiation, EM compatibility, and power electronics problems [5]–[9]. For a large and complex interconnection problem, the PEEC model consists of an excessively large number of partial elements, whose simulation time is prohibitively long because multiple large-scale matrix inversions are involved. Besides, it is difficult for the designers to acquire any physical insight by examining the massive discretization mesh-based partial elements. Nonetheless, a PEEC model can serve as a good starting point to derive a much concise and physically meaningful circuit for frequency-domain simulations [10]–[12]. However, these micromodeling circuits cannot be used for time-domain simulation due to their poor passivity conditions.

To facilitate time-domain analysis of system responses of a large-scale EM problem, various model order reduction (MOR) methods have been developed since the 1990s. The methods can be classified into two categories according to their objectives: macromodeling and micromodeling. The macromodeling attempts to extract a concise model represented by a set of state-space equations while preserving the input–output characteristics of the original problem [13]. Usually, a macromodel does not have a direct correspondence with the physical layout of the problem. On the other hand, the micromodeling provides a circuit domain representation that comes with certain physical meaning. The proposed PEEC-based micromodeling circuit finds an *RLC* circuit that describes the EM effects of a physical interconnection problem [10]–[12].

Many macromodeling methods [13]–[20] have been developed. The well-known Lanczos and Arnoldi algorithms, a subclass of the so-called Krylov subspace methods, constitute the framework of modern MOR research. The main idea of these mathematics-based MOR methods is to find a projection of a large-scale state-space system onto a lower dimensional subspace by a set of appropriate basis vectors [20]. Although the projected lower order state-space system can reserve certain mathematic properties, such as passivity, causality, and reciprocity, it lacks direct physical interpretation of the original EM problem.

The Micromodeling methods that are based on node elimination include AMOR [21], TICER [22], and SIP [23]. The AMOR method [21] is based on observation that those adjacent nodes of the *RC* circuits with almost the same voltage can be aggregated together as a “super node,” which is not suitable for PEEC circuit with coupled *RLC* elements. The TICER approach [22] uses the *Y*– $\Delta$  transformation to reduce

Manuscript received August 15, 2017; revised October 28, 2017; accepted November 15, 2017. Date of publication December 18, 2017; date of current version March 5, 2018. This work was supported by the University Grants Committee of Hong Kong under Grant AoE/P-04/08. (Corresponding author: Ke-Li Wu.)

The authors are with the Department of Electronic Engineering, Chinese University of Hong Kong, Hong Kong (e-mail: yhdou@ee.cuhk.edu.hk; klwu@ee.cuhk.edu.hk).

Color versions of one or more of the figures in this paper are available online at <http://ieeexplore.ieee.org>.

Digital Object Identifier 10.1109/TMTT.2017.2779484

a general *RLC* circuit including inductive couplings for the first time. Similar concept is independently developed for a general PEEC circuit with coupled inductors and coupled capacitors for embedded RF passive designs [10], [11]. The SIP method [23] for *RLC* circuit is a projection method mathematically, but its implementation is similar to the node elimination-based method. However, these methods will introduce a large amount of redundant branches during node eliminate process, and require two large-scale matrix inversions in order to obtain a reducible inductance and capacitance matrices from the PEEC model.

Recently, a direct mesh-based micromodeling method for the PEEC model was proposed [12]. The method overcomes two critical issues faced with the Y- $\Delta$  transformation-based micromodeling methods: 1) the scalability issue constrained by matrix inversions of large-order inductance and potance matrices and 2) the proxy direct inductance for the actual mutual inductances of the original problem. In the micromodeling circuit [12], the circuit nodes are in correspondence with the physical layout and the accuracy in terms of frequency-domain responses can be specified by the user. However, the micromodeling circuit in [12] may generate negative self-inductances due to missing some critical inductive components in the circuit transformation, which causes instability issues in time-domain simulation.

In this paper, an improved micromodeling method is proposed to overcome the nonpassivity problem. Different from the previous micromodeling methods, the proposed method introduces a pseudoinductor for each grounded potors to retain the inductive components more accurately in the MOR process. At the end of the micromodeling process, the pseudoinductors will be internalized by regular inductors. It is demonstrated through numerical examples that by introducing the pseudoinductor, the improved micromodeling circuit is in higher conformity with the original PEEC model than the existing micromodeling circuits. The numerical results show that the proposed micromodeling circuit ensures all the self-inductances to be positive, and the passivity violation factor of the proposed micromodeling circuit is smaller than that of the existing method [12] by three orders of magnitude. Most importantly, a new passivity check and enforcement method for a general *RLC* circuit is proposed to systematically correct the numerical error in a nonpassive circuit model so that the passivity of the circuit model can be guaranteed for time-domain simulation.

In addition to maintain higher fidelity of the physical meaning of an EM problem in the circuit model, this improved micromodeling method inherits the two most attractive attributes from [12]: 1) high scalability, i.e., there is no matrix inversion or decomposition involved in the modeling process and 2) high suitability of being accelerated by the GPU parallel computation.

In this paper, the rigorous derivation of the proposed micromodeling method, the passivity check and enforcement method and the scheme for the GPU parallel computation will be discussed in detail. The numerical results demonstrate that the computational time for SI analysis of a practical high-speed interconnection problem using the proposed micromodeling

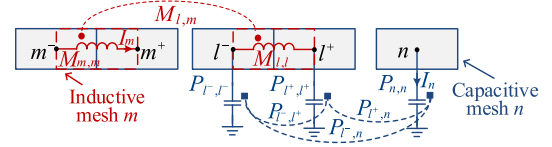


Fig. 1. PEEC meshes and their circuit representation.

circuit is about three orders of magnitude less than that if a traditional PEEC model is used.

Without loss of generality, this paper only concerns the quasi-static EM problems, in which the electrical size of the circuit cannot be too large so that the radiation effect can be neglected.

## II. PEEC REPRESENTATION OF AN EM PROBLEM

The PEEC model is a circuit representation of the discretized MPIE [3]. The quasi-static MPIE for infinitely thin conductors can be expressed as

$$\mathbf{E}(\mathbf{r}) = -j\omega \int_{s'} \bar{\bar{G}}_A(\mathbf{r}, \mathbf{r}') \cdot \mathbf{J}(\mathbf{r}') ds' - \nabla \int_{s'} G_\phi(\mathbf{r}, \mathbf{r}') \rho(\mathbf{r}') ds' \quad (1)$$

where  $\bar{\bar{G}}_A$  and  $G_\phi$  are Green's functions of magnetic vector and electric scalar potentials, respectively; and  $\rho$  and  $\mathbf{J}$  are the surface charges and current densities, respectively.

Without loss of generality, only the *x*-component in (1) is considered. Discretizing the conductor surface for the current and charge densities using PEEC meshes, as shown in Fig. 1, then applying Galerkin's matching procedure on an inductive mesh *l*, the discretized form of (1) is given by

$$\frac{I_l}{\sigma w_l} I_l^x + \sum_m \frac{j\omega}{w_l w_m} \left[ \iint G_A^{xx}(\mathbf{r}, \mathbf{r}') ds'_m ds_l \right] I_m^x + \sum_n \left[ \frac{\iint G_\phi(\mathbf{r}, \mathbf{r}') ds'_n ds_{l+}}{a_{l+} a_n} - \frac{\iint G_\phi(\mathbf{r}, \mathbf{r}') ds'_n ds_{l-}}{a_{l-} a_n} \right] Q_n = 0 \quad (2)$$

where mesh *m*, *l* are inductive meshes and *w* is the width of an inductive mesh; mesh *n*, *l*<sup>-</sup> and *l*<sup>+</sup> are capacitive meshes and *a* is the area of a capacitive mesh; and indexes *l*<sup>-</sup> and *l*<sup>+</sup> are two terminals of inductive cell *l* with current *I<sub>l</sub>* flowing from node *l*<sup>-</sup> to node *l*<sup>+</sup>. A finite-difference approximation has been used for the derivative operator appearing in the third term of (2). In a circuit-oriented form, (2) is represented as

$$R_l I_l + \sum_m j\omega M_{l,m} I_m + \sum_n (P_{l+,n} - P_{l-,n}) Q_n = 0 \quad (3)$$

where constant  $M_{l,m}$  is the partial (self- or mutual) inductance between inductive cells *l* and *m*; *I<sub>m</sub>* is the current flowing through the inductive cell *m*; constant  $P_{l\pm,n}$  is the coefficient of electric potential between capacitive cells *l*<sup>±</sup> and *n*; and *Q<sub>n</sub>* is the total charge on the capacitive cell *n*. For ease of the micromodeling, conductor loss *R<sub>l</sub>* is conflated with the

corresponding self-inductance  $M_{l,m}$  and  $Q_n$  is replaced by  $I_n/j\omega$ , (3) becomes

$$\sum_m j\omega M_{l,m} I_m + \sum_n (P_{l^+,n} - P_{l^-,n}) I_n / j\omega = 0. \quad (4)$$

In an analogous manner to conventional definitions of self-inductance of an inductor and mutual inductance of two inductors, quantity  $P_{i,i}$  is called as self-potance of the circuit element potior  $i$  and  $P_{i,j}$  is called as mutual potance of two potiors  $i$  and  $j$ . Equation (4) can be interpreted by the circuit in Fig. 1, in which inductors are coupled with each other and potiors are coupled with each other as well. For clarity, mutual inductance and mutual potance are represented by circular dots and square dots, respectively. The proposed micromodeling method deals with potance matrix and inductance matrix directly.

### III. THEORY OF MICROMODELING METHOD

A good micromodeling method based on the PEEC model should possess the following three desired attributes: 1) it must be passive; 2) it contains as much physical essence of the original EM problem as possible; and 3) it is highly suitable for GPU parallel computation.

However, the micromodeling method in [12] proposed for frequency-domain analysis is not favoring in attribute 1 due to its inevitable negative self-inductances. This issue is overcome by this improved micromodeling method. Fig. 2 outlines the micromodeling process. Fig. 2(a) shows a conventional PEEC model. In step 1, pseudoinductors are introduced to the PEEC model, as shown in Fig. 2(b), which are critical to preserve accurate inductive components in the micromodeling process. In step 2, a recursive process for absorbing an insignificant node is conducted. The process first finds the most insignificant node (MIN), say, node  $k$  in Fig. 2(b), in a low-pass sense, then the node is absorbed by a new equivalent circuit transformation, as illustrated in Fig. 2(c). Having had the node absorbed, the shunt branches generated in the circuit transformation need to be combined, as illustrated in Fig. 2(d). Repeating step 2 until all insignificant nodes are absorbed and a concise circuit model is obtained as the one shown in Fig. 2(e). In step 3, the pseudoinductors are internalized by surrounding regular inductors, as shown in Fig. 2(f). Finally, in step 4, the passivity of the micromodeling circuit is checked and enforced if necessary. As a result, a passive and concise micromodeling circuit is obtained. The theories for the four-step process are explicated in the following sections.

#### A. Introducing Pseudoinductors for PEEC Model

The proposed method adds a pseudoinductor in series with each grounded potior at the beginning of the micromodeling process, as shown in Fig. 2(b). To distinguish with the pseudoinductors, the inductors that are defined by inductive meshes are called regular inductor. Having had the pseudoinductors introduced in the process of absorbing the insignificant node  $k$ , as shown in Fig. 2(b), the voltages of the neighboring nodes of node  $k$  are able to remain the same in the circuit transformation, as shown in Fig. 2(c). As a result, the method

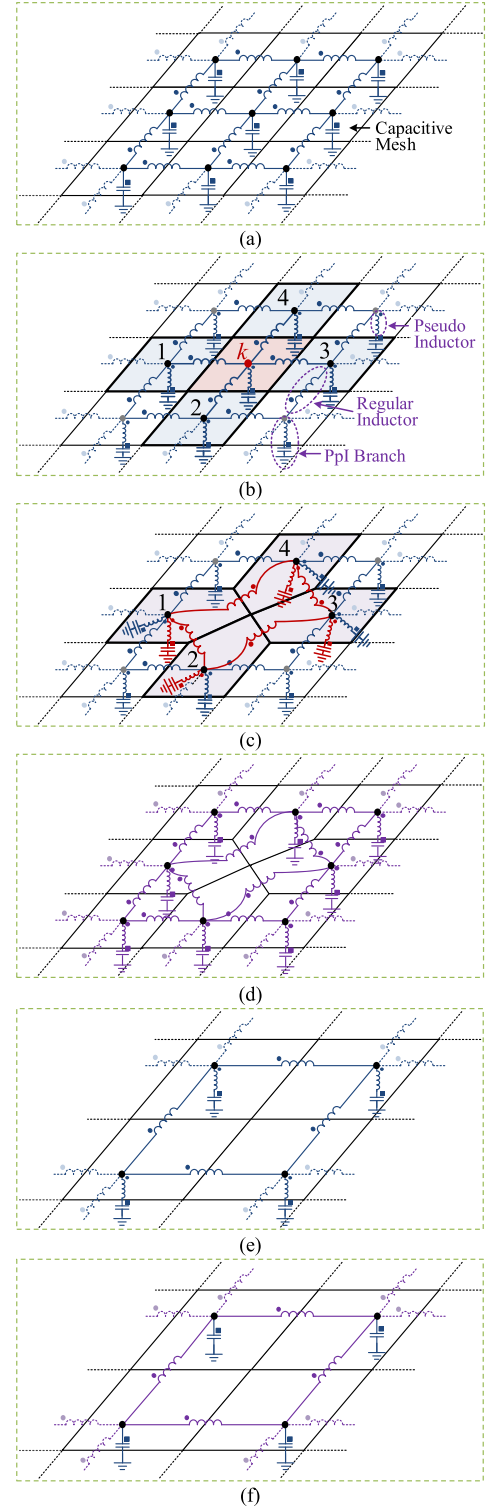


Fig. 2. Illustration of the proposed micromodeling method. (a) Mesh and circuit topology of PEEC model. (b) Finding the MIN  $k$ . (c) Circuit transformation to absorb node  $k$ . (d) Combining coupled shunt branches. (e) Mesh and circuit topology after absorbing all insignificant nodes. (f) Internalizing pseudoinductors by regular inductors.

preserves more physical essence in the node absorbing process than that in [12]. The initial values of pseudoinductors are set to zero and they will be updated after absorbing each insignificant node. In the end of micromodeling, these pseudoinductors

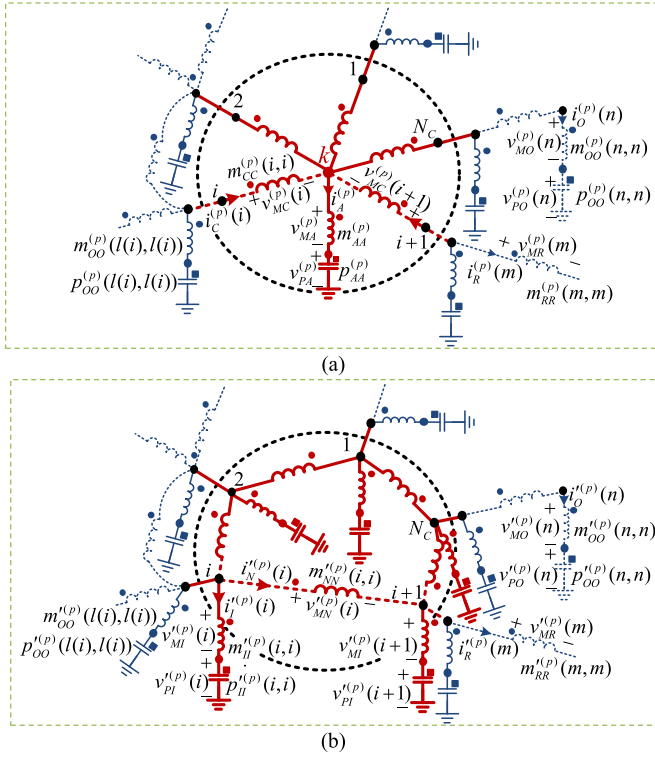


Fig. 3. Circuit transformation for absorbing an insignificant node. (a) Circuit prior to transformation. (b) Circuit posterior to transformation.

will be internalized by regular inductors as shown in Fig. 2(f), because the pseudoinductors are actually contributed by the regular inductors.

For convenience, the branch of a potior serially connected with a pseudoinductor is called as a potior-pseudoinductor branch, or a PpI branch.

### B. Hypotheses of Circuit Transformation

The new circuit transformation concerns absorbing a node in accordance with a physical sensible remeshing scheme, as illustrated in Fig. 2(b) and (c). Assuming that node  $k$  in Fig. 3(a) is the MIN to be absorbed at the  $p$ th step of the recursive node absorbing process, following hypotheses and definitions are given, referring to Fig. 3(a) and (b) with node  $k$  being absorbed.

- 1) Assume the potior and pseudoinductor associated with node  $k$  as well as all the inductors connecting to node  $k$  are to be assimilated; they are called assimilated potior, assimilated inductor, and connecting inductors, respectively.
- 2) An incremental PpI branch is added to each of the  $N_c$  neighboring nodes to share one- $N$ th portion of the potance of mesh  $k$ . The potors and inductors in the added PpI branches are called incremental potors and incremental inductors, respectively.
- 3) A new inductor is introduced between each consecutive pair of the neighboring nodes, reflecting the newly introduced current paths. The newly introduced inductors are called new inductors.

- 4) All mutual couplings associated with the assimilated elements are transferred to the mutual couplings with the newly added elements.
- 5) Unchanged potors and pseudoinductors are named as other potors and other inductors, respectively. Their associated PpI branches are called other branches.
- 6) Unchanged regular inductors are named as remaining inductors.

The notations and voltage–current relations of the circuit variables in the circuit transformation are defined as follows.

- 1) The potance matrix  $\mathbf{P}^{(p)}$  before node  $k$  being absorbed is defined by voltage vector  $\mathbf{v}_p^{(p)}$  and current vector  $\mathbf{i}_p^{(p)}$  as

$$\begin{bmatrix} \mathbf{v}_{PO}^{(p)} \\ \mathbf{v}_{PA}^{(p)} \end{bmatrix} = \frac{1}{j\omega} \begin{bmatrix} \mathbf{P}_{OO}^{(p)} & \mathbf{P}_{OA}^{(p)} \\ (\mathbf{P}_{OA}^{(p)})^T & \mathbf{P}_{AA}^{(p)} \end{bmatrix} \begin{bmatrix} \mathbf{i}_O^{(p)} \\ \mathbf{i}_A^{(p)} \end{bmatrix} \quad (5)$$

where subscripts  $O$  and  $A$  refer to the other and the assimilated potors, respectively.

- 2) The inductance matrix  $\mathbf{M}^{(p)}$  before node  $k$  being absorbed is defined by voltage vector  $\mathbf{v}_M^{(p)}$  and current vector  $\mathbf{i}_M^{(p)}$  as

$$\begin{bmatrix} \mathbf{v}_{MR}^{(p)} \\ \mathbf{v}_{MO}^{(p)} \\ \mathbf{v}_{MC}^{(p)} \\ \mathbf{v}_{MA}^{(p)} \end{bmatrix} = j\omega \begin{bmatrix} \mathbf{M}_{RR}^{(p)} & (\mathbf{M}_{OR}^{(p)})^T & (\mathbf{M}_{CR}^{(p)})^T & \mathbf{m}_{RA}^{(p)} \\ \mathbf{M}_{OR}^{(p)} & \mathbf{M}_{OO}^{(p)} & (\mathbf{M}_{CO}^{(p)})^T & \mathbf{m}_{OA}^{(p)} \\ \mathbf{M}_{CR}^{(p)} & \mathbf{M}_{CO}^{(p)} & \mathbf{M}_{CC}^{(p)} & \mathbf{m}_{CA}^{(p)} \\ (\mathbf{m}_{RA}^{(p)})^T & (\mathbf{m}_{OA}^{(p)})^T & (\mathbf{m}_{CA}^{(p)})^T & m_{AA}^{(p)} \end{bmatrix} \begin{bmatrix} \mathbf{i}_R^{(p)} \\ \mathbf{i}_O^{(p)} \\ \mathbf{i}_C^{(p)} \\ \mathbf{i}_A^{(p)} \end{bmatrix} \quad (6)$$

where subscripts  $R$ ,  $O$ ,  $C$ , and  $A$  refer to the remaining inductors, the other inductors, the connecting inductors, and the assimilated inductors, respectively.

- 3) The potance matrix  $\mathbf{P}'^{(p)}$  after node  $k$  being absorbed is defined by voltage vector  $\mathbf{v}'_p^{(p)}$  and current vector  $\mathbf{i}'_p^{(p)}$  as

$$\begin{bmatrix} \mathbf{v}'_{PO}^{(p)} \\ \mathbf{v}'_{PI}^{(p)} \end{bmatrix} = \frac{1}{j\omega} \begin{bmatrix} \mathbf{P}'_{OO}^{(p)} & (\mathbf{P}'_{IO}^{(p)})^T \\ \mathbf{P}'_{IO}^{(p)} & \mathbf{P}'_{II}^{(p)} \end{bmatrix} \begin{bmatrix} \mathbf{i}'_O^{(p)} \\ \mathbf{i}'_I^{(p)} \end{bmatrix} \quad (7)$$

where subscripts  $O$  and  $I$  refer to the other potors and the incremental potors, respectively.

- 4) The inductance matrix  $\mathbf{M}'^{(p)}$  after node  $k$  being absorbed is defined by voltage vector  $\mathbf{v}'_M^{(p)}$  and current vector  $\mathbf{i}'_M^{(p)}$



as

$$\underbrace{\begin{bmatrix} \mathbf{v}_{MR}^{(p)} \\ \mathbf{v}_{MO}^{(p)} \\ \mathbf{v}_{MN}^{(p)} \\ \mathbf{v}_{MI}^{(p)} \end{bmatrix}}_{\mathbf{v}_M^{(p)}} = j\omega \underbrace{\begin{bmatrix} \mathbf{M}_{RR}^{(p)} & (\mathbf{M}_{OR}^{(p)})^T & (\mathbf{M}_{NR}^{(p)})^T & (\mathbf{M}_{IR}^{(p)})^T \\ \mathbf{M}_{OR}^{(p)} & \mathbf{M}_{OO}^{(p)} & (\mathbf{M}_{NO}^{(p)})^T & (\mathbf{M}_{IO}^{(p)})^T \\ \mathbf{M}_{NR}^{(p)} & \mathbf{M}_{NO}^{(p)} & \mathbf{M}_{NN}^{(p)} & (\mathbf{M}_{IN}^{(p)})^T \\ \mathbf{M}_{IR}^{(p)} & \mathbf{M}_{IO}^{(p)} & \mathbf{M}_{IN}^{(p)} & \mathbf{M}_{II}^{(p)} \end{bmatrix}}_{\mathbf{M}^{(p)}} \underbrace{\begin{bmatrix} \mathbf{i}_R^{(p)} \\ \mathbf{i}_O^{(p)} \\ \mathbf{i}_N^{(p)} \\ \mathbf{i}_I^{(p)} \end{bmatrix}}_{\mathbf{i}_M^{(p)}} \quad (8)$$

where subscripts  $R, O, N$ , and  $I$  refer to the remaining inductors, the other inductors, the new inductors and the incremental inductors, respectively.

- 5) Let  $\mathbf{a}$  be a column vector, whose  $i$ th element is  $a(i)$ . Define the  $N$ -by-1 vector  $\tilde{\mathbf{a}}$  that is related to the  $N$ -by-1 vector  $\mathbf{a}$  by

$$\tilde{a}(i) = a(i\%N + 1) \quad (9)$$

where modulo operation  $i\%N$  finds the remainder after division of  $i$  by  $N$ . For example,  $1\%2 = 1$  and  $2\%2 = 0$ .

- 6) Let  $\mathbf{B}$  be a matrix, whose element in  $i$ th row and  $j$ th column is expressed as  $b(i, j)$ . Define  $N$ -by- $N$  matrices  $\tilde{\mathbf{B}}, \bar{\mathbf{B}}$  and  $\hat{\mathbf{B}}$  that are related to an  $N$ -by- $N$  matrix  $\mathbf{B}$  by

$$\begin{aligned} \tilde{b}(i, j) &= b(i\%N + 1, j) \\ \bar{b}(i, j) &= b(i, j\%N + 1) \\ \hat{b}(i, j) &= b(i\%N + 1, j\%N + 1). \end{aligned} \quad (10)$$

- 7) Let  $\mathbf{j}_N$  be an  $N$ -by-1 vector and  $\mathbf{J}_N$  be an  $N$ -by- $N$  matrix, whose elements are all one. Let  $\mathbf{I}_N$  be an  $N$ -by- $N$  identity matrix. For example

$$\mathbf{j}_2 = \begin{bmatrix} 1 \\ 1 \end{bmatrix} \quad \mathbf{J}_2 = \begin{bmatrix} 1 & 1 \\ 1 & 1 \end{bmatrix} \quad \mathbf{I}_2 = \begin{bmatrix} 1 & 0 \\ 0 & 1 \end{bmatrix}. \quad (11)$$

### C. Equivalence for the Circuit Transformation

The following equivalent conditions are imposed on the proposed circuit transformation:

- 1) Referring Fig. 3(a) and (b), equivalent KVL and KCL conditions for the transformation are

$$\mathbf{v}_{PI}^{(p)} + \mathbf{v}_{MI}^{(p)} = \mathbf{v}_{MC}^{(p)} + \mathbf{j}_{Nc} v_{MA}^{(p)} + \mathbf{j}_{Nc} v_{PA}^{(p)} \quad (12a)$$

$$\mathbf{v}_{MN}^{(p)} = \mathbf{v}_{MC}^{(p)} - \bar{\mathbf{v}}_{MC}^{(p)} \quad (12b)$$

$$\tilde{\mathbf{i}}_N^{(p)} - \mathbf{i}_N^{(p)} + \tilde{\mathbf{i}}_I^{(p)} = \tilde{\mathbf{i}}_C^{(p)} \quad (13a)$$

$$\mathbf{j}_{Nc}^T \mathbf{i}_I^{(p)} = \mathbf{i}_A^{(p)} \quad (13b)$$

$$N_C \mathbf{i}_I^{(p)} = \mathbf{i}_A^{(p)} \mathbf{j}_{Nc}. \quad (13c)$$

- 2) The voltages and currents across and through the other pots, other inductors and remaining inductors are unchanged, that is,

$$\mathbf{v}_{PO}^{(p)} = \mathbf{v}_{PO}^{(p)} \quad \mathbf{v}_{MO}^{(p)} = \mathbf{v}_{MO}^{(p)} \quad \mathbf{v}_{MR}^{(p)} = \mathbf{v}_{MR}^{(p)} \quad (14a)$$

$$\mathbf{i}_O^{(p)} = \mathbf{i}_O^{(p)} \quad \mathbf{i}_R^{(p)} = \mathbf{i}_R^{(p)}. \quad (14b)$$

### D. Circuit Transformation

The following discussions derives the proposed circuit transformation.

1) *Updating Formulas Related to Incremental Elements:* According to (7) and (8), the voltages across the incremental PpI branches are

$$\begin{aligned} \mathbf{v}_{MI}^{(p)} + \mathbf{v}_{PI}^{(p)} &= j\omega [\mathbf{M}_{IR}^{(p)} \mathbf{i}_R^{(p)} + \mathbf{M}_{IO}^{(p)} \mathbf{i}_O^{(p)} + \mathbf{M}_{IN}^{(p)} \mathbf{i}_N^{(p)} + \mathbf{M}_{II}^{(p)} \mathbf{i}_I^{(p)}] \\ &\quad + (1/j\omega) [\mathbf{P}_{IO}^{(p)} \mathbf{i}_O^{(p)} + \mathbf{P}_{II}^{(p)} \mathbf{i}_I^{(p)}]. \end{aligned} \quad (15a)$$

According to (12a), (5), and (6), one can further find that

$$\begin{aligned} \mathbf{v}_{MI}^{(p)} + \mathbf{v}_{PI}^{(p)} &= \mathbf{v}_{MC}^{(p)} + \mathbf{j}_{Nc} v_{MA}^{(p)} + \mathbf{j}_{Nc} v_{PA}^{(p)} \\ &= j\omega [\mathbf{M}_{CR}^{(p)} \mathbf{i}_R^{(p)} + \mathbf{M}_{CO}^{(p)} \mathbf{i}_O^{(p)} + \mathbf{M}_{CC}^{(p)} \mathbf{i}_C^{(p)} + \mathbf{m}_{CA}^{(p)} \mathbf{i}_A^{(p)}] \\ &\quad + j\omega \mathbf{j}_{Nc} [(\mathbf{m}_{RA}^{(p)})^T \mathbf{i}_R^{(p)} + (\mathbf{m}_{OA}^{(p)})^T \mathbf{i}_O^{(p)} + (\mathbf{m}_{CA}^{(p)})^T \mathbf{i}_C^{(p)} \\ &\quad + \mathbf{m}_{AA}^{(p)} \mathbf{i}_A^{(p)}] + (1/j\omega) \mathbf{j}_{Nc} [(\mathbf{p}_{OA}^{(p)})^T \mathbf{i}_O^{(p)} + \mathbf{p}_{AA}^{(p)} \mathbf{i}_A^{(p)}]. \end{aligned} \quad (15b)$$

By using (13), (15b) can be expressed as

$$\begin{aligned} \mathbf{v}_{MI}^{(p)} + \mathbf{v}_{PI}^{(p)} &= j\omega [\mathbf{M}_{CR}^{(p)} + \mathbf{j}_{Nc} (\mathbf{m}_{RA}^{(p)})^T] \mathbf{i}_R^{(p)} \\ &\quad + j\omega [\mathbf{M}_{CO}^{(p)} + \mathbf{j}_{Nc} (\mathbf{m}_{OA}^{(p)})^T] \mathbf{i}_O^{(p)} \\ &\quad + j\omega [\mathbf{M}_{CC}^{(p)} - \tilde{\mathbf{M}}_{CC}^{(p)} + \mathbf{j}_{Nc} (\mathbf{m}_{CA}^{(p)})^T - \mathbf{j}_{Nc} (\bar{\mathbf{m}}_{CA}^{(p)})^T] \mathbf{i}_N^{(p)} \\ &\quad + j\omega [\mathbf{M}_{CC}^{(p)} + \mathbf{j}_{Nc} (\mathbf{m}_{CA}^{(p)})^T + \mathbf{m}_{CA}^{(p)} \mathbf{j}_{Nc}^T + N_C \mathbf{m}_{AA}^{(p)} \mathbf{I}_{Nc}] \mathbf{i}_I^{(p)} \\ &\quad + (1/j\omega) [\mathbf{j}_{Nc} (\mathbf{p}_{OA}^{(p)})^T \mathbf{i}_O^{(p)} + N_C \mathbf{p}_{AA}^{(p)} \mathbf{I}_{Nc} \mathbf{i}_I^{(p)}]. \end{aligned} \quad (15c)$$

Comparing the right-hand sides of (15a) and (15c), the updating formulas for the circuit elements related to the incremental elements are obtained as

$$\mathbf{M}_{IR}^{(p)} = \mathbf{M}_{CR}^{(p)} + \mathbf{j}_{Nc} (\mathbf{m}_{RA}^{(p)})^T \quad (16a)$$

$$\mathbf{M}_{IO}^{(p)} = \mathbf{M}_{CO}^{(p)} + \mathbf{j}_{Nc} (\mathbf{m}_{OA}^{(p)})^T \quad (16b)$$

$$\mathbf{M}_{IN}^{(p)} = \mathbf{M}_{CC}^{(p)} - \tilde{\mathbf{M}}_{CC}^{(p)} + \mathbf{j}_{Nc} (\mathbf{m}_{CA}^{(p)})^T - \mathbf{j}_{Nc} (\bar{\mathbf{m}}_{CA}^{(p)})^T \quad (16c)$$

$$\mathbf{M}_{II}^{(p)} = \mathbf{M}_{CC}^{(p)} + \mathbf{j}_{Nc} (\mathbf{m}_{CA}^{(p)})^T + \mathbf{m}_{CA}^{(p)} \mathbf{j}_{Nc}^T + N_C \mathbf{m}_{AA}^{(p)} \mathbf{I}_{Nc} \quad (16d)$$

$$\mathbf{P}_{IO}^{(p)} = \mathbf{j}_{Nc} (\mathbf{p}_{OA}^{(p)})^T \quad (16e)$$

$$\mathbf{P}_{II}^{(p)} = N_C \mathbf{p}_{AA}^{(p)} \mathbf{I}_{Nc}. \quad (16f)$$

2) *Updating Formulas Related to New Inductors:* According to (8), the voltages of the new inductors are

$$\begin{aligned} \mathbf{v}_{MN}^{(p)} &= j\omega [\mathbf{M}_{NR}^{(p)} \mathbf{i}_R^{(p)} + \mathbf{M}_{NO}^{(p)} \mathbf{i}_O^{(p)} + \mathbf{M}_{NN}^{(p)} \mathbf{i}_N^{(p)} + (\mathbf{M}_{IN}^{(p)})^T \mathbf{i}_I^{(p)}]. \end{aligned} \quad (17a)$$

According to (12b), the above voltages can be expressed as

$$\begin{aligned} \mathbf{v}'_{MN}(p) &= \mathbf{v}_{MC}(p) - \bar{\mathbf{v}}_{MC}(p) \\ &= j\omega [\mathbf{M}_{CR}^{(p)} \mathbf{i}_R^{(p)} + \mathbf{M}_{CO}^{(p)} \mathbf{i}_O^{(p)} + \mathbf{M}_{CC}^{(p)} \mathbf{i}_C^{(p)} + \mathbf{m}_{CA}^{(p)} \mathbf{i}_A^{(p)}] \\ &\quad - j\omega [\bar{\mathbf{M}}_{CR}^{(p)} \mathbf{i}_R^{(p)} + \bar{\mathbf{M}}_{CO}^{(p)} \mathbf{i}_O^{(p)} + \bar{\mathbf{M}}_{CC}^{(p)} \mathbf{i}_C^{(p)} + \bar{\mathbf{m}}_{CA}^{(p)} \mathbf{i}_A^{(p)}]. \end{aligned} \quad (17b)$$

Substituting (13a) and (13b), (17b) becomes

$$\begin{aligned} \mathbf{v}'_{MN}(p) &= j\omega [\mathbf{M}_{CR}^{(p)} - \bar{\mathbf{M}}_{CR}^{(p)}] \mathbf{i}'_R^{(p)} + j\omega [\mathbf{M}_{CO}^{(p)} - \bar{\mathbf{M}}_{CO}^{(p)}] \mathbf{i}'_O^{(p)} \\ &\quad + j\omega [\mathbf{M}_{CC}^{(p)} - \bar{\mathbf{M}}_{CC}^{(p)} - \bar{\mathbf{M}}_{CC}^{(p)} + \hat{\mathbf{M}}_{CC}^{(p)}] \mathbf{i}'_N^{(p)} \\ &\quad + j\omega [\mathbf{M}_{CC}^{(p)} - \bar{\mathbf{M}}_{CC}^{(p)} + \mathbf{m}_{CA}^{(p)} \mathbf{j}_{Nc}^T - \bar{\mathbf{m}}_{CA}^{(p)} \mathbf{j}_{Nc}^T] \mathbf{i}'_I^{(p)}. \end{aligned} \quad (17c)$$

Comparing the right-hand sides of (17a) and (17c), the updating formulas of elements related to the new inductors are obtained as

$$\mathbf{M}'_{NR}(p) = \mathbf{M}_{CR}^{(p)} - \bar{\mathbf{M}}_{CR}^{(p)} \quad (18a)$$

$$\mathbf{M}'_{NO}(p) = \mathbf{M}_{CO}^{(p)} - \bar{\mathbf{M}}_{CO}^{(p)} \quad (18b)$$

$$\mathbf{M}'_{NN}(p) = \mathbf{M}_{CC}^{(p)} - \bar{\mathbf{M}}_{CC}^{(p)} - \bar{\mathbf{M}}_{CC}^{(p)} + \hat{\mathbf{M}}_{CC}^{(p)} \quad (18c)$$

$$\mathbf{M}'_{IN}(p) = \mathbf{M}_{CC}^{(p)} - \bar{\mathbf{M}}_{CC}^{(p)} + \mathbf{j}_{Nc} (\mathbf{m}_{CA}^{(p)})^T - \mathbf{j}_{Nc} (\bar{\mathbf{m}}_{CA}^{(p)})^T. \quad (18d)$$

Formulas (16c) and (18d) for updating  $\mathbf{M}'_{IN}(p)$  are the same, which shows that the proposed circuit transformation is symmetric.

3) *Circuit Elements Related to Other Potors, Other Inductors, and Remaining Inductors:* Using the same derivation method, it can be concluded that the other potors, other inductors, remaining inductors, as well as the mutual couplings between these circuit elements are not changed after the circuit transformation. That is,

$$\mathbf{P}'_{OO}(p) = \mathbf{P}_{OO}(p) \quad \mathbf{M}'_{OO}(p) = \mathbf{M}_{OO}(p) \quad \mathbf{M}'_{RR}(p) = \mathbf{M}_{RR}(p) \quad \mathbf{M}'_{OR}(p) = \mathbf{M}_{OR}(p). \quad (19)$$

### E. Combining Coupled Shunt Branches

After the circuit transformation, each incremental PpI branch is in shunt with an other PpI branch and a new inductor branch is possibly in shunt with a remaining inductor branch. Every two shunt connected branches need to be combined as shown in Fig. 2(d) before absorbing the next insignificant node.

Referring to Fig. 4, consider shunt connected branch *S* and branch *I*, which can be a pair of PpI branches or a pair of inductor branches and will be combined as branch *S*. The elements in the two branches are not only coupled to each other but are also coupled to the rest of circuit elements. PpI branches and inductor branches in the rest of circuit are distinguished by subscripts *O* and *R*, respectively. When the shunt branches are combined, all the mutual impedances in the circuit need to be updated. According to [12], the combined circuit elements as well as the concerned mutual couplings can be directly written here for the sack of brevity.

1) The self-impedance of combined branch *S* is

$$z'_{SS} = 1/y_t. \quad (20a)$$

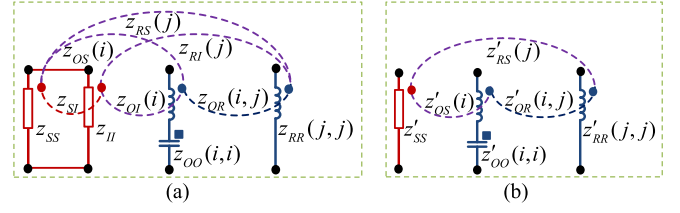


Fig. 4. Combining process of two coupled shunt branches. (a) Circuit with two coupled shunt branches. (b) Circuit posterior to combining the coupled shunt branches.

2) The mutual impedances between combined branch *S* and remaining inductor branches or other PpI branches are

$$\mathbf{z}'_{RS} = [(y_{SS} + y_{SI}) \mathbf{z}_{RS} + (y_{II} + y_{SI}) \mathbf{z}_{RI}] / y_t \quad (20b)$$

$$\mathbf{z}'_{OS} = [(y_{SS} + y_{SI}) \mathbf{z}_{OS} + (y_{II} + y_{SI}) \mathbf{z}_{OI}] / y_t. \quad (20c)$$

3) The mutual impedances among other PpI branches and remaining inductor branches are

$$\mathbf{Z}'_{OO} = \mathbf{Z}_{OO} - \frac{y_{SS} y_{II} + y_{SI}^2}{y_t} (\mathbf{z}_{OS} - \mathbf{z}_{OI}) (\mathbf{z}_{OS} - \mathbf{z}_{OI})^T \quad (20d)$$

$$\mathbf{Z}'_{OR} = \mathbf{Z}_{OR} - \frac{y_{SS} y_{II} + y_{SI}^2}{y_t} (\mathbf{z}_{OS} - \mathbf{z}_{OI}) (\mathbf{z}_{RS} - \mathbf{z}_{RI})^T \quad (20e)$$

$$\mathbf{Z}'_{RR} = \mathbf{Z}_{RR} - \frac{y_{SS} y_{II} + y_{SI}^2}{y_t} (\mathbf{z}_{RS} - \mathbf{z}_{RI}) (\mathbf{z}_{RS} - \mathbf{z}_{RI})^T \quad (20f)$$

where  $\begin{bmatrix} y_{SS} & y_{SI} \\ y_{SI} & y_{II} \end{bmatrix} = \begin{bmatrix} z_{SS} & z_{SI} \\ z_{SI} & z_{II} \end{bmatrix}^{-1}$  and  $y_t = y_{SS} + y_{II} + 2y_{SI}$ .

A general updating formula for inductance matrix and potance matrix can be derived from (20). Specific expressions for different types of shunt branches will be different.

1) *Two Shunt Connected PpI Branches:* When the shunt branches are PpI branches, the concerned inductance matrix and potance matrix of the circuit before combining can be expressed as

$$\begin{aligned} \mathbf{M} &= \begin{bmatrix} \mathbf{M}_{RR} & \mathbf{M}_{OR}^T & \mathbf{m}_{RS} & \mathbf{m}_{RI} \\ \mathbf{M}_{OR} & \mathbf{M}_{OO} & \mathbf{m}_{OS} & \mathbf{m}_{OI} \\ \mathbf{m}_{RS}^T & \mathbf{m}_{OS}^T & \mathbf{m}_{SS} & \mathbf{m}_{SI} \\ \mathbf{m}_{RI}^T & \mathbf{m}_{OI}^T & \mathbf{m}_{SI} & \mathbf{m}_{II} \end{bmatrix} \\ \mathbf{P} &= \begin{bmatrix} \mathbf{P}_{OO} & \mathbf{p}_{OS} & \mathbf{p}_{OI} \\ \mathbf{p}_{OS}^T & \mathbf{p}_{SS} & \mathbf{p}_{SI} \\ \mathbf{p}_{OI}^T & \mathbf{p}_{SI} & \mathbf{p}_{II} \end{bmatrix} \end{aligned} \quad (21)$$

Similarly, the inductance matrix and potance matrix after combining can be expressed as

$$\begin{aligned} \mathbf{M}' &= \begin{bmatrix} \mathbf{M}'_{RR} & (\mathbf{M}'_{OR})^T & \mathbf{m}'_{RS} \\ \mathbf{M}'_{OR} & \mathbf{M}'_{OO} & \mathbf{m}'_{OS} \\ (\mathbf{m}'_{RS})^T & (\mathbf{m}'_{OS})^T & \mathbf{m}'_{SS} \end{bmatrix} \\ \mathbf{P}' &= \begin{bmatrix} \mathbf{P}'_{OO} & \mathbf{p}'_{OS} \\ (\mathbf{p}'_{OS})^T & \mathbf{p}'_{SS} \end{bmatrix}. \end{aligned} \quad (22)$$

Substituting (21) and (22) into (20) leads to the following relations:

$$\begin{aligned}
 j\omega m'_{SS} + p'_{SS}/j\omega &= j\omega k_1(e_5 - e_1 e_4 e_6 - \omega^2 e_7) + e_1 e_4 / j\omega \\
 j\omega \mathbf{m}'_{RS} &= j\omega k_2 \mathbf{m}_{RS} + j\omega k_3 \mathbf{m}_{RI} \\
 j\omega \mathbf{m}'_{OS} + \mathbf{p}'_{OS}/j\omega &= k_2(j\omega \mathbf{m}_{OS} + \mathbf{p}_{OS}/j\omega) \\
 &\quad + k_3(j\omega \mathbf{m}_{OI} + \mathbf{p}_{OI}/j\omega) \\
 j\omega \mathbf{M}'_{OO} + \mathbf{P}'_{OO}/j\omega &= j\omega \mathbf{M}_{OO} + \mathbf{P}_{OO}/j\omega \\
 &\quad - j\omega k_1(j\omega \mathbf{m}_O + \mathbf{p}_O/j\omega) \\
 &\quad \times (j\omega \mathbf{m}_O + \mathbf{p}_O/j\omega)^T \\
 j\omega \mathbf{M}'_{OR} &= j\omega \mathbf{M}_{OR} - j\omega k_1(j\omega \mathbf{m}_O + \mathbf{p}_O/j\omega) \\
 &\quad \times (j\omega \mathbf{m}_R)^T \\
 j\omega \mathbf{M}'_{RR} &= j\omega \mathbf{M}_{RR} - j\omega k_1(j\omega \mathbf{m}_R)(j\omega \mathbf{m}_R)^T
 \end{aligned} \tag{23}$$

where

$$\begin{aligned}
 c_1 &= \omega^2(m_{SS} + m_{II} - 2m_{SI})/(p_{SS} + p_{II} - 2p_{SI}); \\
 c_2 &= \omega^2(m_{II} - m_{SI})/(p_{II} - p_{SI}); \\
 c_3 &= \omega^2(m_{SS} - m_{SI})/(p_{SS} - p_{SI}); \\
 e_1 &= 1/(p_{SS} + p_{II} - 2p_{SI}), e_2 = e_1(p_{II} - p_{SI}); \\
 e_3 &= e_1(p_{SS} - p_{SI}), e_4 = p_{SS}p_{II} - (p_{SI})^2; \\
 e_5 &= p_{II}m_{SS} + p_{SS}m_{II} - 2p_{SI}m_{SI}, e_6 = m_{SS} + m_{II} - 2m_{SI}; \\
 e_7 &= m_{SS}m_{II} - (m_{SI})^2, k_1 = e_1/(1 - c_1); \\
 k_2 &= e_2(1 - c_2)/(1 - c_1), k_3 = e_3(1 - c_3)/(1 - c_1); \\
 \mathbf{m}_O &= \mathbf{m}_{OS} - \mathbf{m}_{OI}, \mathbf{m}_R = \mathbf{m}_{RS} - \mathbf{m}_{RI}, \mathbf{p}_O = \mathbf{p}_{OS} - \mathbf{p}_{OI}.
 \end{aligned}$$

By comparing the coefficients of  $\omega$  and  $1/\omega$  terms of (23), the following updating formulas for the inductance and potance matrices that transform the circuit in Fig. 4(a) into (b) can be obtained:

$$\begin{aligned}
 m'_{SS} &= k_1(e_5 - e_1 e_4 e_6 - \omega^2 e_7) \quad p'_{SS} = e_1 e_4 \\
 \mathbf{m}'_{OS} &= k_2 \mathbf{m}_{OS} + k_3 \mathbf{m}_{OI} \quad \mathbf{m}'_{RS} = k_2 \mathbf{m}_{RS} + k_3 \mathbf{m}_{RI} \\
 \mathbf{p}'_{OS} &= k_2 \mathbf{p}_{OS} + k_3 \mathbf{p}_{OI} \quad \mathbf{P}'_{OO} = \mathbf{P}_{OO} - k_1 \mathbf{p}_O \mathbf{p}_O^T \\
 \mathbf{M}'_{OO} &= \mathbf{M}_{OO} - k_1(\mathbf{m}_O \mathbf{p}_O^T + \mathbf{p}_O \mathbf{m}_O^T - \omega^2 \mathbf{m}_O \mathbf{m}_O^T) \\
 \mathbf{M}'_{OR} &= \mathbf{M}_{OR} - k_1(\mathbf{p}_O \mathbf{m}_R^T - \omega^2 \mathbf{m}_O \mathbf{m}_R^T) \\
 \mathbf{M}'_{RR} &= \mathbf{M}_{RR} + \omega^2 k_1 \mathbf{m}_R \mathbf{m}_R^T.
 \end{aligned} \tag{24}$$

2) *Two Shunt Connected Inductor Branches*: The case of two shunt connected inductor branches is a special case of two shunt connected PpI branches when potances are absent. Therefore, updating formulas for inductance and potance matrices can be obtained from (24) as

$$\begin{aligned}
 m'_{SS} &= j\omega g_1[m_{SS}m_{II} - (m_{SI})^2] \quad \mathbf{m}'_{OS} = g_2 \mathbf{m}_{OS} + g_3 \mathbf{m}_{OI} \\
 \mathbf{m}'_{RS} &= g_2 \mathbf{m}_{RS} + g_3 \mathbf{m}_{RI} \quad \mathbf{M}'_{OO} = \mathbf{M}_{OO} - g_1 \mathbf{m}_O \mathbf{m}_O^T \\
 \mathbf{M}'_{OR} &= \mathbf{M}_{OR} - g_1 \mathbf{m}_O \mathbf{m}_R^T \quad \mathbf{M}'_{RR} = \mathbf{M}_{RR} - g_1 \mathbf{m}_R \mathbf{m}_R^T \\
 \mathbf{P}'_{OO} &= \mathbf{P}_{OO}
 \end{aligned} \tag{25}$$

where  $g_1 = 1/(m_{SS} + m_{II} - 2m_{SI})$ ,  $g_2 = g_1(m_{II} - m_{SI})$ , and  $g_3 = g_1(m_{SS} - m_{SI})$ .

#### F. Low-Pass Approximation

After combining a pair of shunt PpI branches, the updated elements in (24) contain frequency-dependent terms  $c_1, c_2,$

and  $c_3$ , which are not in conformity with the original PEEC circuit. For a quasi-static problem, the three terms can be approximated to be zero in the low-pass sense. Therefore, the updated circuit elements become constants as

$$\begin{aligned}
 m'_{SS} &= e_1(e_5 - e_1 e_4 e_6) \quad p'_{SS} = e_1 e_4 \\
 \mathbf{m}'_{OS} &= e_2 \mathbf{m}_{OS} + e_3 \mathbf{m}_{OI} \quad \mathbf{m}'_{RS} = e_2 \mathbf{m}_{RS} + e_3 \mathbf{m}_{RI} \\
 \mathbf{p}'_{OS} &= e_2 \mathbf{p}_{OS} + e_3 \mathbf{p}_{OI} \quad \mathbf{P}'_{OO} = \mathbf{P}_{OO} - e_1 \mathbf{p}_O \mathbf{p}_O^T \\
 \mathbf{M}'_{OO} &= \mathbf{M}_{OO} - e_1 \mathbf{m}_O \mathbf{p}_O^T - e_1 \mathbf{p}_O \mathbf{m}_O^T \\
 \mathbf{M}'_{OR} &= \mathbf{M}_{OR} - e_1 \mathbf{p}_O \mathbf{m}_R^T \quad \mathbf{M}'_{RR} = \mathbf{M}_{RR}.
 \end{aligned} \tag{26}$$

Approximating  $c_1, c_2$ , and  $c_3$  terms to zero will cause an approximation error for a non-dc frequency. In the frequency band from 0 to  $\omega_{\max}$ , where  $\omega_{\max}$  is the highest frequency of interest, the upper bound of the low-pass approximation error for combining a pair of PpI branches can be found as

$$\Delta = \omega_{\max}^2 \left[ \frac{|m_{II} - m_{SI}|}{p_{II} - p_{SI}} + \frac{|m_{SS} - m_{SI}|}{p_{SS} - p_{SI}} \right] \tag{27}$$

where the facts that  $(p_{II} - p_{SI})$  and  $(p_{SS} - p_{SI})$  are all nonnegative real values and all self-inductances are complex number whose imaginary part reflect conductor loss are used.

After all the shunt branches are combined and the low-pass approximation is applied, the  $p$ th node absorbing process is completed. The resultant potance matrix and inductance matrix are denoted as  $\mathbf{P}^{(p+1)}$  and  $\mathbf{M}^{(p+1)}$ , respectively.

#### G. Finding the Most Insignificant Node (MIN)

The earlier sections gave the method to absorb the  $p$ th nodes assuming that the MIN had been found at the beginning of the  $p$ th node absorbing process, as shown in Fig. 2(b). In this section, the method to find the MIN will be derived based on that the MIN is the node that will introduce the minimum low-pass approximation error after the node being absorbed. Therefore, to determine the MIN at the  $p$ th iteration, the error bound  $\Delta^{(p)}(k)$  of each node  $k$  needs to be precomputed for the circuit after absorbing the first  $(p-1)$  nodes.

The error bound associated with absorbing each node depends on combining the incremental PpI branches with their respective shunt branches that are PpI branches in the group of “other branches.” Assume the indexes of the incremental PpI branches associated with node  $k$  runs from 1 to  $N_c$ , and indexes of their shunt PpI branches are numbered according to the index mapping array  $l$  in the group of “other branches.” According to (7), (8), and (27), the aggregated error bound for node  $k$  can be expressed as

$$\Delta^{(p)}(k) = \omega_{\max}^2 \sum_{i=1}^{N_c} \left[ \frac{|m'_{II}{}^{(p)}(i, i) - m'_{IO}{}^{(p)}(i, l(i))|}{p'_{II}{}^{(p)}(i, i) - p'_{IO}{}^{(p)}(i, l(i))} + \frac{|m'_{OO}{}^{(p)}(l(i), l(i)) - m'_{IO}{}^{(p)}(i, l(i))|}{p'_{OO}{}^{(p)}(l(i), l(i)) - p'_{IO}{}^{(p)}(i, l(i))} \right]. \tag{28}$$

According to (16), (18), and (19), the error bound for each node can be precomputed using (5), (6), and (28). The node with the smallest error bound is defined as the MIN.

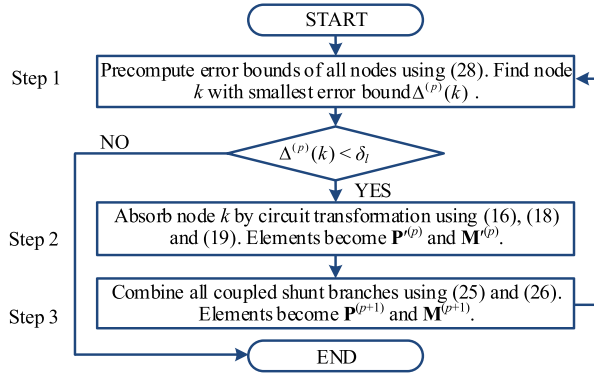


Fig. 5. Flowchart of node absorbing process.

### H. Recursive Node Absorbing Process

The node absorbing process is repeated until no node satisfies the preset accuracy criterion  $\delta_l$  on the error bound. The whole process can be summarized by three steps as demonstrated by the flowchart in Fig. 5.

### I. Internalization of Pseudoinductors

As said, the pseudoinductors are introduced to retain high fidelity of inductive information in the circuit transformation. After all insignificant nodes are absorbed and the recursive process is stopped, all the pseudoinductors will be internalized by rest of regular inductors in one-by-one fashion. Assuming the first  $i-1$  pseudoinductors have been internalized, the process for internalizing pseudoinductor  $i$  is derived here.

The circuit with the  $i$ th pseudoinductor is shown in Fig. 6(a), in which  $N_C$  inductors are connected to node  $i$ . In the context of internalizing the  $i$ th pseudoinductor, the inductors in the circuit can be divided into three groups: 1) the pseudoinductor to be assimilated; 2) the inductors connecting to the pseudoinductor  $i$ ; and 3) rest of the pseudo and regular inductors, which are distinguished by subscripts  $A$ ,  $C$ , and  $R$ , respectively. The overall inductance matrix of the circuit can be sorted in the form of

$$\mathbf{M}^{(i)} = \begin{bmatrix} \mathbf{M}_{RR}^{(i)} & (\mathbf{M}_{CR}^{(i)})^T & \mathbf{m}_{RA}^{(i)} \\ \mathbf{M}_{CR}^{(i)} & \mathbf{M}_{CC}^{(i)} & \mathbf{m}_{CA}^{(i)} \\ (\mathbf{m}_{RA}^{(i)})^T & (\mathbf{m}_{CA}^{(i)})^T & m_{AA}^{(i)} \end{bmatrix}. \quad (29a)$$

The corresponding voltage vector and current vector are denoted as

$$\mathbf{v}^{(i)} = \begin{bmatrix} (\mathbf{v}_R^{(i)})^T & (\mathbf{v}_C^{(i)})^T & v_A^{(i)} \end{bmatrix}^T \quad (29b)$$

$$\mathbf{i}^{(i)} = \begin{bmatrix} (\mathbf{i}_R^{(i)})^T & (\mathbf{i}_C^{(i)})^T & i_A^{(i)} \end{bmatrix}^T \quad (29c)$$

respectively. By definition

$$\mathbf{v}^{(i)} = j\omega \mathbf{M}^{(i)} \mathbf{i}^{(i)}. \quad (29d)$$

Fig. 6(b) shows the circuit with pseudoinductor  $i$  being internalized. The corresponding inductance matrix of the resultant circuit, the voltage vector, and the current vector are sorted

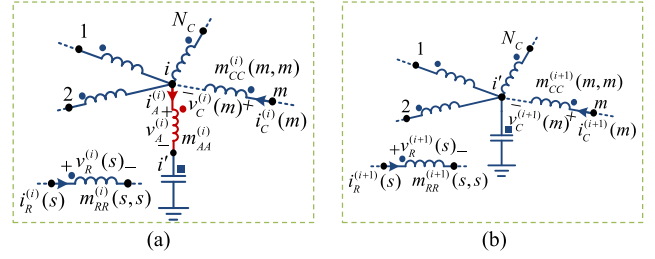


Fig. 6. Illustration of internalizing a pseudoinductor by regular inductors. (a) Circuit prior to internalizing a pseudoinductor. (b) Circuit posterior to internalizing the pseudoinductor.

as

$$\mathbf{M}^{(i+1)} = \begin{bmatrix} \mathbf{M}_{RR}^{(i+1)} & (\mathbf{M}_{CR}^{(i+1)})^T \\ \mathbf{M}_{CR}^{(i+1)} & \mathbf{M}_{CC}^{(i+1)} \end{bmatrix} \quad (30a)$$

$$\mathbf{v}^{(i+1)} = \begin{bmatrix} (\mathbf{v}_R^{(i+1)})^T & (\mathbf{v}_C^{(i+1)})^T \end{bmatrix}^T \quad (30b)$$

$$\mathbf{i}^{(i+1)} = \begin{bmatrix} (\mathbf{i}_R^{(i+1)})^T & (\mathbf{i}_C^{(i+1)})^T \end{bmatrix}^T \quad (30c)$$

respectively. By definition

$$\mathbf{v}^{(i+1)} = j\omega \mathbf{M}^{(i+1)} \mathbf{i}^{(i+1)}. \quad (30d)$$

According to (30), voltage  $\mathbf{v}_C^{(i+1)}$  can be expressed as

$$\mathbf{v}_C^{(i+1)} = j\omega \mathbf{M}_{CR}^{(i+1)} \mathbf{i}_R^{(i+1)} + j\omega \mathbf{M}_{CC}^{(i+1)} \mathbf{i}_C^{(i+1)}. \quad (31)$$

Absorbing pseudoinductor  $i$  needs to satisfy the following equivalent conditions:

$$\mathbf{j}_{N_C}^T \mathbf{i}_C^{(i+1)} = i_A^{(i)} \quad \mathbf{v}_C^{(i+1)} = \mathbf{v}_C^{(i)} + \mathbf{j}_{N_C} v_A^{(i)}. \quad (32)$$

Therefore, the voltage  $\mathbf{v}_C^{(i+1)}$  can be expressed as

$$\begin{aligned} \mathbf{v}_C^{(i+1)} &= j\omega \mathbf{j}_{N_C} [(\mathbf{m}_{RA}^{(i)})^T \mathbf{i}_R^{(i)} + (\mathbf{m}_{CA}^{(i)})^T \mathbf{i}_C^{(i)} + m_{AA}^{(i)} i_A^{(i)}] \\ &\quad + j\omega [\mathbf{M}_{CR}^{(i)} \mathbf{i}_R^{(i)} + \mathbf{M}_{CC}^{(i)} \mathbf{i}_C^{(i)} + \mathbf{m}_{CA}^{(i)} i_A^{(i)}] \\ &= j\omega [\mathbf{M}_{CC}^{(i)} + \mathbf{j}_{N_C} (\mathbf{m}_{CA}^{(i)})^T + \mathbf{m}_{CA} \mathbf{j}_{N_C}^T + m_{AA}^{(i)} \mathbf{j}_{N_C}] \mathbf{i}_C^{(i+1)} \\ &\quad + j\omega [\mathbf{M}_{CR}^{(i)} + \mathbf{j}_{N_C} (\mathbf{m}_{RA}^{(i)})^T] \mathbf{i}_R^{(i+1)}. \end{aligned} \quad (33)$$

Comparing the right-hand sides of (31) and (32) leads to the following updating formulas:

$$\begin{aligned} \mathbf{M}_{CC}^{(i+1)} &= \mathbf{M}_{CC}^{(i)} + \mathbf{j}_{N_C} (\mathbf{m}_{CA}^{(i)})^T + \mathbf{m}_{CA} \mathbf{j}_{N_C}^T + m_{AA}^{(i)} \mathbf{j}_{N_C} \\ \mathbf{M}_{CR}^{(i+1)} &= \mathbf{M}_{CR}^{(i)} + \mathbf{j}_{N_C} (\mathbf{m}_{RA}^{(i)})^T \quad \mathbf{M}_{RR}^{(i+1)} = \mathbf{M}_{RR}^{(i)}. \end{aligned} \quad (34)$$

A micromodeling circuit without pseudoinductors can be obtained after all pseudoinductors are internalized.

### J. Computational Overhead and Parallel Computation

In the recursive micromodeling process, the shunt branches combining process dominates computational overhead. As can be found from (25) and (26) that the computations mainly compose of outer products of two vectors in the form of

$$\mathbf{Z} = \mathbf{Z} + c\mathbf{x} \cdot \mathbf{y}^T \quad (35)$$

where  $\mathbf{Z}$  is an  $m$ -by- $m$  matrix, which is a placeholder for inductance matrix  $\mathbf{M}$  and potance matrix  $\mathbf{P}$ ,  $\mathbf{x}$  and  $\mathbf{y}$  are



$m$ -by-1 vectors,  $c$  is a constant, and  $m$  represents the number of inductors or potors. The computational overhead of each combining process is in the order of  $O(m^2)$ . Let  $N$  be the number of recursive iteration and  $M$  be the maximum order of the inductance or potance matrix, the computational overhead of the whole micromodeling process is in the order of  $O(NM^2)$ .

There are  $m^2$  arithmetic operations for each outer product, which can be computed in parallel using multicores CPU or GPU. It turns out to be a good news because the future trend in developing computing devices will continue to concentrate on multicores rather than the performance of a single thread [36]. That means the micromodeling method can fully utilize the advances on parallel computation, especially on GPUs.

To utilize GPU efficiently in developing the micromodeling circuit, two more works need to be done: 1) the amount and frequency of data transactions between CPU and GPU need to be minimized and 2) the amount and frequency of data transactions (read/write) inside GPU need to be minimized.

By using the strategies developed recently [37], [38], the proposed micromodeling process can be accelerated by about 30 times as compared to a single CPU process. The numerical examples will demonstrate the superiority of the micromodeling method by adoption of GPU parallel computations.

#### IV. PASSIVITY CHECKING AND ENFORCEMENT

Unlike the conventional passivity enforcement methods [24]–[30], which are applicable to the state-space matrices of a macro or micromodel but the amended system is not recoverable to a circuit model, the new passivity checking and enforcement method is applicable to a general physically meaningful  $RLC$  circuit model, with which while the passivity of the micromodeling circuit is warranted the original circuit configuration is also retained.

Let  $\mathbf{R}$ ,  $\mathbf{M}$ , and  $\mathbf{P}$  be the resistance matrix, inductance matrix, and potance matrix. According to [31], the cumulative energy at time  $t$  of the general  $RLC$  circuit can be found as

$$W(t) = \int_0^t \mathbf{i}_R^T(\tau) \mathbf{R} \mathbf{i}_R(\tau) d\tau + \frac{1}{2} \mathbf{i}_L^T(t) \mathbf{M} \mathbf{i}_L(t) + \frac{1}{2} \mathbf{q}_P^T(t) \mathbf{P} \mathbf{q}_P(t) \quad (36)$$

where  $\mathbf{i}_R$  and  $\mathbf{i}_L$  are vectors of currents flowing through the resistors and inductors, respectively; and  $\mathbf{q}_P$  is the vector of charges on the potors.

The passivity constraint is derived from the passivity definition that the cumulative energy of a circuit is nonnegative at all times and for all possible excitation signals [13], which leads to

*Corollary:* A general  $RLC$  circuit is passive if and only if its resistance matrix  $\mathbf{R}$ , inductance matrix  $\mathbf{M}$ , and potance matrix  $\mathbf{P}$  are all positive semidefinite, or equivalently the eigenvalues of matrices  $\mathbf{R}$ ,  $\mathbf{M}$ , and  $\mathbf{P}$  are nonnegative.

The corollary not only provides a constraint to check the passivity, but also implies that a nonpassive  $RLC$  circuit can be remediated directly by ensuring its resistance matrix  $\mathbf{R}$ , inductance matrix  $\mathbf{M}$ , and potance matrix  $\mathbf{P}$  to be positive

semidefinite matrices. There are some effective enforcement methods for a nonpositive semidefinite matrix [33]–[35]. A simple modified Cholesky algorithm [34] is used, where a generic symmetric matrix  $\mathbf{F}$  is used as a placeholder for  $\mathbf{R}$ ,  $\mathbf{M}$ , and  $\mathbf{P}$ . The eigen decomposition of the  $N$ -by- $N$  matrix  $\mathbf{F}$  can be expressed as

$$\mathbf{F} = \mathbf{V} \mathbf{\Lambda} \mathbf{V}^T, \mathbf{\Lambda} = \text{diag}(\lambda_1, \dots, \lambda_N) \quad (37)$$

where matrices  $\mathbf{V}$  and  $\mathbf{\Lambda}$  are the eigenvector matrix and eigenvalue diagonal matrix of matrix  $\mathbf{F}$ , respectively.

By adding a corrective matrix  $\Delta \mathbf{F}$ , matrix  $\mathbf{F}$  is enforced to be a positive semidefinite matrix. The corrective matrix is

$$\Delta \mathbf{F} = \mathbf{V} \Delta \mathbf{\Lambda} \mathbf{V}^T, \Delta \mathbf{\Lambda} = \text{diag}(\Delta \lambda_1, \dots, \Delta \lambda_N) \quad (38)$$

where the  $i$ th diagonal value  $\Delta \lambda_i$  of  $\Delta \mathbf{\Lambda}$  is constructed by

$$\Delta \lambda_i = \begin{cases} 0, & \lambda_i \geq 0 \\ -\lambda_i, & \lambda_i < 0 \end{cases}, \quad i = 1, 2, \dots, N. \quad (39)$$

The Frobenius norm [32] of  $\Delta \mathbf{F}$  is defined to quantify the passivity violation factor of matrix  $\mathbf{F}$

$$\|\Delta \mathbf{F}\|_F^2 = \sqrt{\sum_{i=1}^N \Delta \lambda_i^2}. \quad (40)$$

Obviously, the larger the Frobenius norm is, the severer the nonpassivity of the circuit model is. The passivity enforcement scheme is suitable for a physically meaningful micromodeling circuit, whose passivity violation is usually caused by numerical errors and is very small. The numerical examples show that the passivity violation factor of the inductance matrix  $\mathbf{M}$  of the micromodeling circuit is smaller than that of the method in [12] by three orders of magnitude.

#### V. NUMERICAL EXAMPLES

In this section, two examples are used to demonstrate the versatility, scalability, and accuracy of the micromodeling method for high-speed/frequency interconnection and packaging problems. The first example is a low-order PEEC model of an LTCC bandpass filter, which is used to demonstrate the high fidelity of the micromodeling method in preserving the physical essence of the original EM problem. The second example is a multilayer and multiport interconnection circuit with a large-order PEEC model. This example is used to show the scalability and the ability of GPU acceleration of the proposed method.

In all numerical examples, the PEEC models are quasi-static and a mixed rectangular and triangular meshing scheme is used. The micromodeling, the PEEC, and the Passive Reduced-Order Interconnect Macromodeling Algorithm (PRIMA) models are executed using single core on a PC with Intel(R) Core(TM) i7-3770 CPU at 3.4 GHz. To demonstrate the suitability of the micromodeling method for GPU acceleration, the GPU module of Nvidia Geforce GTX 980 Ti with 2816 cores is used for demonstration purpose.

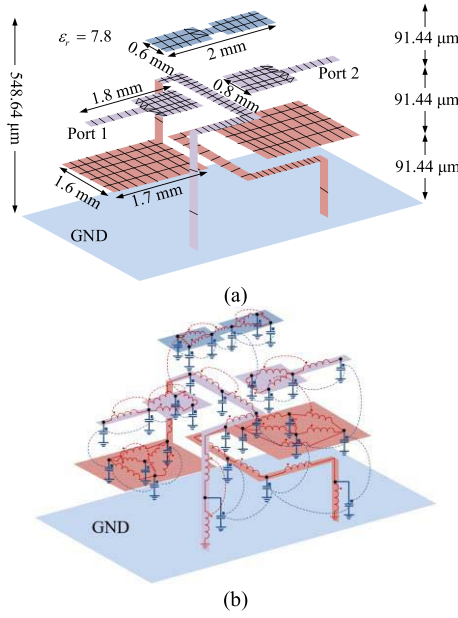


Fig. 7. Example of a lossless multilayer LTCC bandpass filter. (a) Circuit layout and meshing scheme. (b) Derived micromodeling circuit.

#### A. Example 1: LTCC Bandpass Filter

The first example is an LTCC multilayer bandpass filter as depicted in Fig. 7(a). The filter consists of three metal layers. The dielectric constant and geometric dimensions are marked in Fig. 7(a). Infinitely thin perfect conductor is assumed.

The original PEEC model is generated from the meshing scheme superimposed in Fig. 7(a). Details of the PEEC model are listed in Table I. The order of the PEEC model is reduced by one order of magnitude by both the proposed micromodeling method and the method in [12]. The two micromodeling circuits are compared in the aspects of circuit size, S-parameters, system poles, passivity, and time-domain simulation results.

In deriving the proposed micromodeling circuit, the low-pass approximation criterion  $\delta_l$  is set to 0.02 and the low-pass cutoff frequency is chosen to be 5 GHz. The micromodeling circuit is superimposed on the filter layout in Fig. 7(b), showing a clear look of its physical meaning.

The S-parameters of the two micromodeling circuits are compared with that of the original PEEC model and that of Agilent RF momentum module (ADS) commercial software (RF momentum module) in Fig. 8(a) and (b). Both the magnitude and phase of the S-parameters simulated by these methods agree well in the frequency range of interest from 0.1 to 5 GHz. To make a quasi-static approximation, the multilayer full-wave Green's function at 10 MHz is used in the PEEC modeling.

The system poles of the admittance matrix [16] of the two micromodeling circuits are compared with those of the PEEC model in Table II. The system pole frequencies in some representative steps of the recursive process are listed in ascending order from the most significant frequency (corresponding to the smallest pole) to the least significant frequency. It can be observed that, after absorbing the least important node at a recursive step, the significant system

TABLE I  
CIRCUIT SIZE OF PEEC MODEL, METHOD IN [12], AND THIS METHOD

	PEEC model	Method in [12]	This method
Circuit order	612	76	75
No. of nodes	245	33	32
No. of ports	243	31	30
No. of capacitive couplings	29,403	465	435
No. of inductors	365	41	41
No. of inductive couplings	66,430	820	820
Computing time	7 sec	2 sec	3 sec
S-parameter simulation time (99 frequency points)	22 sec	< 1 sec	< 1 sec
Time-domain simulation time (200 frequency points)	3 sec	< 1 sec	< 1 sec
Passivity violation factor of $\mathbf{M}$ matrix	0	$5.6121 \times 10^{-10}$	$3.9675 \times 10^{-26}$
No. of negative self-inductors	0	23	0

TABLE II  
CHANGE OF SYSTEM POLES DURING RECURSIVE PROCESS (UNIT: GHz)

	The Recursive Process Step Index							
Pole Index	PEEC	This Method				Method in [12]		
	0 <sub>th</sub>	210 <sub>th</sub>	211 <sub>th</sub>	212 <sub>th</sub>	213 <sub>th</sub>	210 <sub>th</sub>	211 <sub>th</sub>	212 <sub>th</sub>
1	2.2198	2.2179	2.2190	2.2181	2.2192	2.2276	2.2290	2.2277
2	2.5539	2.5633	2.5646	2.5630	2.5663	2.5650	2.5661	2.5670
3	7.7583	7.8586	7.8598	7.8443	7.8378	7.5814	7.5777	7.5810
...	...	...	...	...	...	...	...	...
29	63.494	102.64	112.51	186.56	203.98	103.93	118.31	215.04
30	65.260	112.51	186.56	203.98		118.31	215.11	222.86
31	68.226	186.57	203.99			215.11	222.87	
32	68.743	203.99				222.87		
...	...							
242	465.56							

poles are nearly unchanged and the most insignificant pole is digested and assimilated by the next few least important poles. By comparing the errors of the first three significant system poles of the two micromodeling circuits (i.e., the hatched columns in Table II) with those of the original PEEC model, it can be concluded that the proposed micromodeling circuit introduces smaller errors than those of [12], meaning that physical essence of the PEEC model is better preserved than the existing micromodeling circuit.

Passivity violation of the two micromodeling circuits are also compared. The proposed micromodeling circuit does not have any negative self-inductances and the passivity violation factor of its  $\mathbf{M}$  matrix is  $3.9675 \times 10^{-26}$ . However, the micromodeling circuit in [12] has 23 negative self-inductances and the passivity violation factor of its  $\mathbf{M}$  matrix is  $5.6121 \times 10^{-10}$ . In this case, the passivity violation factor of  $\mathbf{M}$  matrix for the original PEEC model is zero.

The time-domain responses simulated by the MNA method [4] of the two micromodeling circuits without any passivity enforcement are compared in Fig. 8(c). The input pulse applied at port 1 is with data rate of 1 Gbit/s and rising/falling edges of 0.1 ns. The output signals of the PEEC model and this method match each other very well, while the output signal by the method in [12] does not converge.

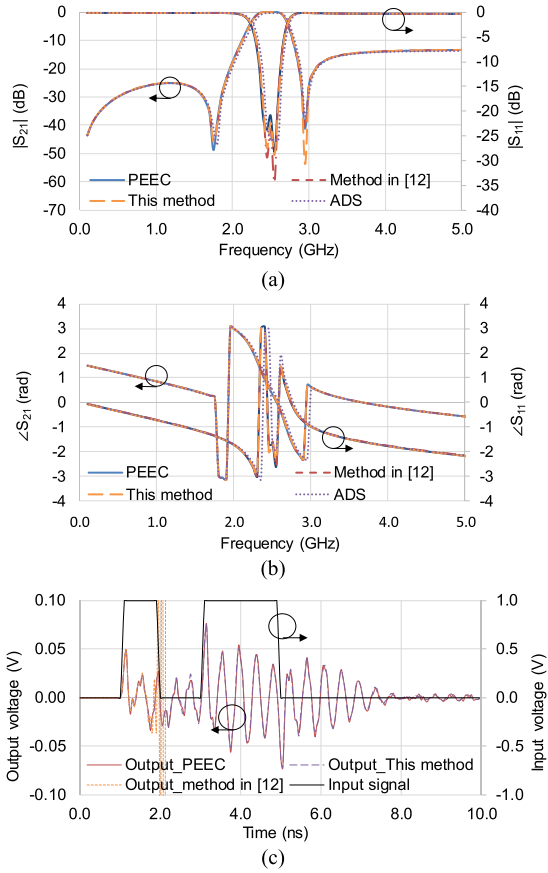


Fig. 8. S-parameters obtained by PEEC model, method in [12], this method, and ADS with (a) magnitude and (b) phase. (c) Time-domain response of PEEC model, method in [12], and this method.

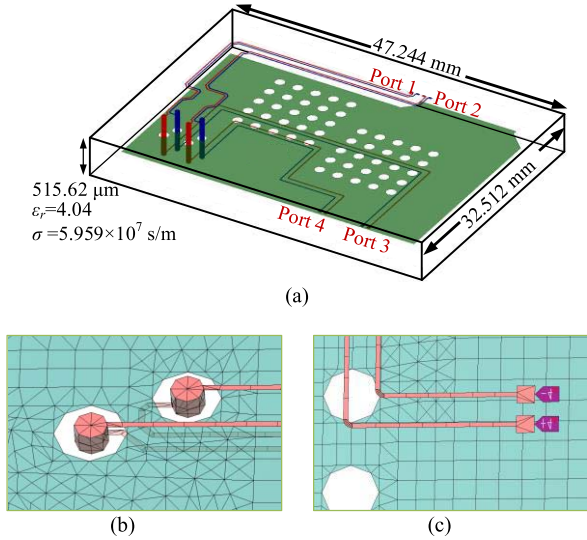


Fig. 9. A lossy multiport multilayer PCB circuit. (a) Circuit layout. (b) Mesh details of via holes. (c) Mesh details of differential lines.

### B. Example 2: Multilayer Interconnection Circuit

To demonstrate the scalability, a typical multiport and multilayer interconnection circuit is considered and is shown in Fig. 9(a). On the circuit board, port 1 and port 2 are the

TABLE III  
COMPARISON OF CIRCUIT SIZES FOR EXAMPLE 2

	PEEC model	Method in [12]	This method
No. of nodes	7,542	858	859
No. of ports	7,534	850	851
No. of capacitive couplings	28,376,811	360,852	361,675
No. of inductors	12,120	1,384	1,711
No. of inductive couplings	73,441,140	957,036	1,462,905
Passivity violation factor of $\mathbf{M}$ matrix	$1.8243 \times 10^{-13}$	$1.0534 \times 10^{-8}$	$6.7500 \times 10^{-11}$
No. of Negative self-inductors	0	592	0
The order of PRIMA model	2574	N/A	N/A

two pairs of differential input terminals and port 3 and port 4 are the differential output terminals. The overall dimensions of the circuit is  $47.244 \times 32.512 \times 515.62 \mu\text{m}$  and the dielectric constant is 4.04. The circuit consists of one layer of power plate and two layers of signal traces connected through via holes. The metal thickness is  $12 \mu\text{m}$  and conductivity is set to  $5.959 \times 10^7 \text{ S} \cdot \text{m}^{-1}$ . Zoomed-in views of via holes and differential signal lines are shown in Fig. 9(b) and (c), respectively. Details of the PEEC model are listed in Table III.

Based on the PEEC model, the derived micromodeling circuit contains only 859 nodes as listed in Table III. The low-pass criterion  $\delta_l$  is set to 0.03 and the highest frequency of interest is set to 5 GHz. The micromodeling process executed by one core CPU takes 156 min 42 s. The modeling time is reduced to 4 min 46 s by a 2816-core GPU, showing that the proposed method is very suitable for GPU parallel computation. For a reference, if the order of the PEEC model is reduced to the same level by the PRIMA method [16], the PRIMA MOR process costs 286 min 11 s using one CPU core.

The simulated S-parameters by the proposed model is compared with those obtained by the original PEEC model, the PRIMA order-reduced model, and the EM simulation of the interconnection circuit layout by ADS, as shown in Fig. 10(a)–(d). The S-parameters of the three models agree well in the frequency range of 0 to 5 GHz. However, the simulation time for the micromodeling circuit and the PEEC model is 4 min 39 s and 1598 min 13 s, respectively. It is expected that as the size of the original PEEC circuit is reduced by about one order of magnitude, the simulation time for the circuit response is reduced about three orders of magnitude. For reference, the simulation time by ADS, which is executed by four CPU cores, is 337 min 13 s.

Before conducting time-domain simulation, the passivity check needs to be done for the circuit model. It is found that the passivity violation factors for the  $\mathbf{M}$  matrix of the original PEEC model and the derived micromodeling circuit are  $1.8243 \times 10^{-13}$  and  $6.7500 \times 10^{-11}$ , respectively, although the factors for  $\mathbf{P}$  and  $\mathbf{R}$  matrices are zero. The micromodeling circuit derived by the method in [12] contains 592 negative self-inductances, the passivity violation factor of its  $\mathbf{M}$  matrix is  $1.0534 \times 10^{-8}$ , and the three orders of magnitude larger than that of the circuit model by the proposed

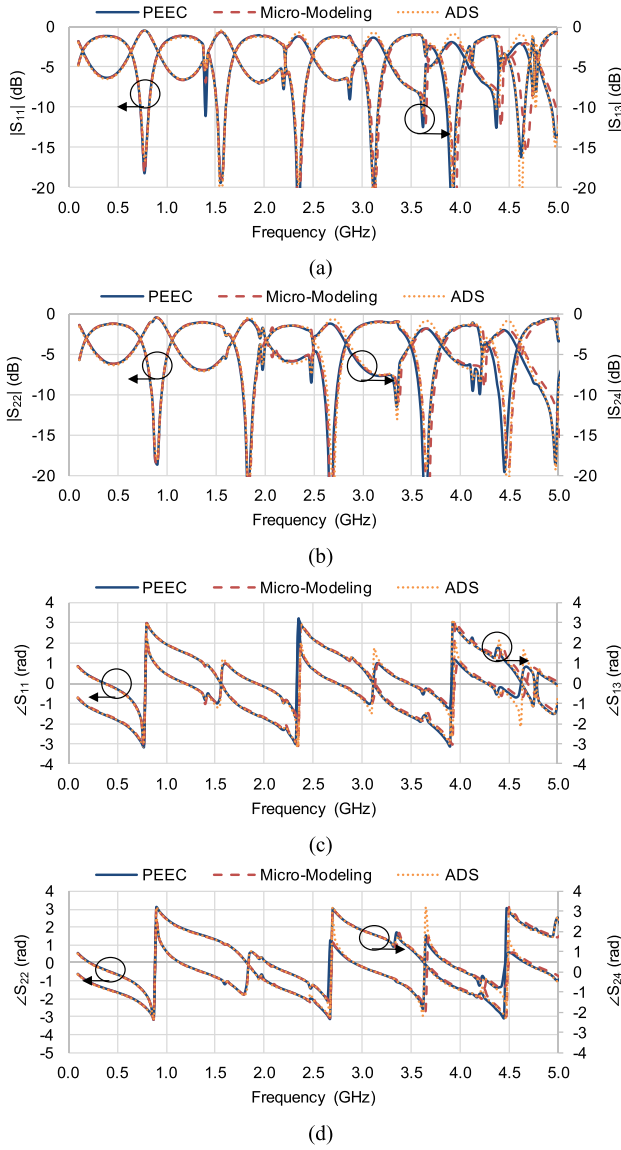


Fig. 10. S-parameters obtained by PEEC model, this method, ADS, and PRIMA. (a) Magnitude of S-parameters  $S_{11}$  and  $S_{13}$ . (b) Magnitude of S-parameters  $S_{22}$  and  $S_{24}$ . (c) Phase of S-parameters  $S_{11}$  and  $S_{13}$ . (d) Phase of S-parameters  $S_{22}$  and  $S_{24}$ .

method. The passivity condition of the PEEC model and the proposed micromodeling circuit is enforced with computing time of 522 min 38 s and 16 s, respectively.

Having had the passivity of the circuits enforced, a sequence of pulse with data rate of 1 Gbit/s and rising/falling edges of 0.1 ns is applied at port 1 while port 2 is terminated by a matched load. The output responses at ports 3 and 4 are simulated by the MNA method. The time-domain responses at port 3 simulated by the passivity enforced PEEC model and the micromodeling circuit are compared in Fig. 11(a), showing very good agreement. However, as shown in Table IV, simulation time of the micromodeling circuit is three orders of magnitude less than that of the PEEC model.

The circuit responses with multiple inputs from multiple ports are straightforward. The advantage of this attribute is obvious for the simulation of eye-diagrams, which usually

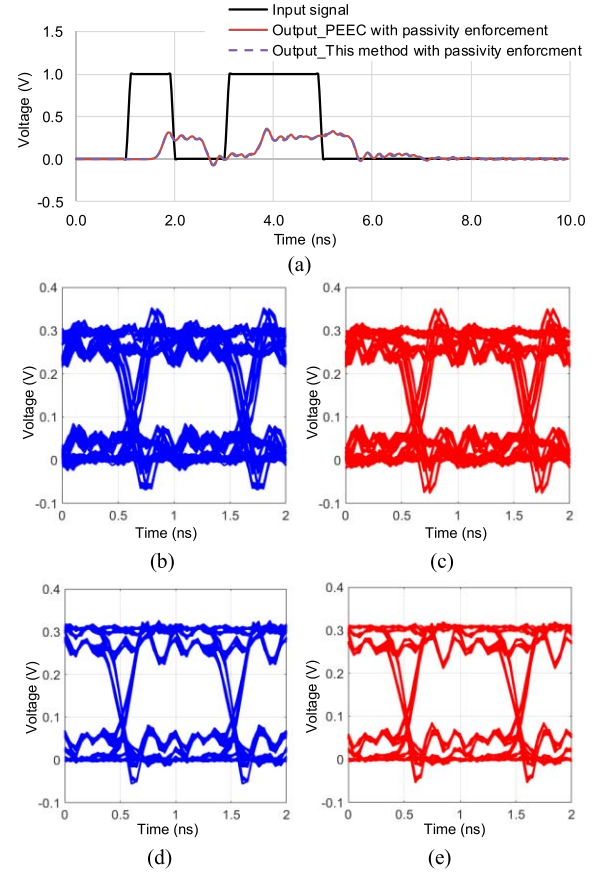


Fig. 11. Responses of the lossy multilayer multiport interconnection circuit. (a) Responses of a pulse input between ports 1 and 3 simulated by PEEC and the micromodeling circuit. (b) Eye diagram at port 3 by the PEEC model. (c) Eye diagram at port 3 by this micromodeling circuit. (d) Eye diagram at port 4 by the PEEC model. (e) Eye diagram at port 4 by this micromodeling circuit. In eye-diagram simulations, ports 1 and 2 are input ports.

TABLE IV  
COMPARISON OF COMPUTATION TIME FOR EXAMPLE 2

	PEEC model	This method
Modeling time using 1 CPU core	11 min 49 sec	156 min 42 sec
Modeling time by a 2816-core GPU	N/A	4 min 46 sec
Passivity enforcement time	522 min 38 sec	16 sec
S-parameters Simulation (197 frequency points)	1,598 min 13 sec	4 min 39 sec
Time-domain simulation (200 time points)	591 min 9 sec	1 min 19 sec
Eye-diagram simulation (5120 time points)	14,942 min 49 sec	34 min 15 sec
S-parameter simulation by ADS RF module (197 frequencies by 4 CPU cores)	337 min 13 sec	
PRIMA modeling time using 1 CPU core	286 min 11 sec	

involves a long pseudorandom binary sequence (PRBS) with different input situations. When the input signals are applied at ports 1 and 2 using a 256-bit PRBS with the same data rate and the rising/falling edge as the short pulse response for Fig. 11(a), the eye-diagrams of the output responses at ports 3 and 4 are simulated by the passivity enforced PEEC model and the micromodeling circuit as shown



in Fig. 11(b)–(e). The eye-diagram simulation of the PEEC model costs 14 942 min 49 s (more than ten days). The simulation time is reduced to 34 min 15 s by adopting the micromodeling circuit using the proposed method.

## VI. CONCLUSION

This paper presents a derived micromodeling circuit for time-domain simulation of a high-speed interconnection and packaging problem. The derivation process of the physically meaningful concise circuit model is straightforward and does not involve any matrix inversion or decomposition. The process is highly suitable for GPU parallel computation. Compared to existing micromodeling methods, by introducing the pseudoinductor to each grounded port, the physical essence of the original PEEC model can be accurately retained in the circuit transformation. Since the method can reduce the size of a PEEC model by nearly one order of magnitude, the simulation time for both frequency- and time-domain responses can be reduced by about three orders of magnitude. To make the circuit model applicable for time-domain simulation, a pertinent passivity check and enforcement method is also proposed to guarantee the passivity of the derived micromodeling circuit. Two numerical examples are given to demonstrate the versatility, scalability, accuracy, and simplicity of the proposed method through the comparisons of simulation results with the PEEC model, an existing micromodeling circuit method, and the classical Krylov-based PRIMA MOR models. It is expected that the micromodeling circuit will provide a very effective tool for time-domain simulation of high-speed interconnection and packaging problems.

## REFERENCES

- [1] *Fundamentals of Signal Integrity*, Tektronix, Beaverton, OR, USA, 2009, p. 2.
- [2] J. Fan, X. Ye, J. Kim, B. Archambeault, and A. Orlandi, "Signal integrity design for high-speed digital circuits: Progress and directions," *IEEE Trans. Electromagn. Compat.*, vol. 52, no. 2, pp. 392–400, May 2010.
- [3] A. E. Ruehli, "Equivalent circuit models for three dimensional multi-conductor systems," *IEEE Trans. Microw. Theory Techn.*, vol. MTT-22, no. 3, pp. 216–221, Mar. 1974.
- [4] C.-W. Ho, A. Ruehli, and P. Brennan, "The modified nodal approach to network analysis," *IEEE Trans. Circuits Syst.*, vol. CAS-22, no. 6, pp. 504–509, Jun. 1975.
- [5] A. E. Ruehli and A. C. Cangellaris, "Progress in the methodologies for the electrical modeling of interconnects and electronic packages," *Proc. IEEE*, vol. 89, no. 5, pp. 740–771, May 2001.
- [6] V. Vahrenholt, H.-D. Brüns, and H. Singer, "Fast EMC analysis of systems consisting of PCBs and metallic antenna structures by a hybridization of PEEC and MoM," *IEEE Trans. Electromagn. Compat.*, vol. 52, no. 4, pp. 962–973, Nov. 2010.
- [7] L. K. Yeung and K.-L. Wu, "Generalized partial element equivalent circuit (PEEC) modeling with radiation effect," *IEEE Trans. Microw. Theory Techn.*, vol. 59, no. 10, pp. 2377–2384, Oct. 2011.
- [8] L. K. Yeung and K.-L. Wu, "PEEC modeling of radiation problems for microstrip structures," *IEEE Trans. Antennas Propag.*, vol. 61, no. 7, pp. 3648–3655, Jul. 2013.
- [9] D. Daroui and J. Ekman, "PEEC-based simulations using iterative method and regularization technique for power electronic applications," *IEEE Trans. Electromagn. Compat.*, vol. 56, no. 6, pp. 1448–1456, Dec. 2014.
- [10] J. Wang and K.-L. Wu, "A derived physically expressive circuit model for multilayer RF embedded passives," *IEEE Trans. Microw. Theory Techn.*, vol. 54, no. 5, pp. 1961–1968, May 2006.
- [11] H. Hu, K. Yang, K. L. Wu, and W. Y. Yin, "Quasi-static derived physically expressive circuit model for lossy integrated RF passives," *IEEE Trans. Microw. Theory Techn.*, vol. 56, no. 8, pp. 1954–1961, Aug. 2008.
- [12] Y. Dou and K.-L. Wu, "Direct mesh-based model order reduction of PEEC model for quasi-static circuit problems," *IEEE Trans. Microw. Theory Techn.*, vol. 64, no. 8, pp. 2409–2422, Jul. 2016.
- [13] S. Grivet-Talocia and B. Gustavsen, "Passivity," in *Passive Macromodeling: Theory and Applications*, 1st ed. Hoboken, NJ, USA: Wiley, 2016, pp. 6–13.
- [14] L. T. Pillage and R. A. Rohrer, "Asymptotic waveform evaluation for timing analysis," *IEEE Trans. Comput.-Aided Design Integr. Circuits Syst.*, vol. 9, no. 4, pp. 352–366, Apr. 1990.
- [15] P. Feldmann and R. W. Freund, "Efficient linear circuit analysis by Padé approximation via the Lanczos process," *IEEE Trans. Comput.-Aided Des. Integr. Circuits Syst.*, vol. 14, no. 5, pp. 639–649, May 1995.
- [16] A. Odabasioglu, M. Celik, and L. T. Pileggi, "PRIMA: Passive reduced-order interconnect macromodeling algorithm," *IEEE Trans. Comput.-Aided Des. Integr. Circuits Syst.*, vol. 17, no. 8, pp. 645–654, Aug. 1998.
- [17] F. Ferranti, G. Antonini, T. Dhaene, and L. Knockaert, "Guaranteed passive parameterized model order reduction of the partial element equivalent circuit (PEEC) method," *IEEE Trans. Electromagn. Compat.*, vol. 52, no. 4, pp. 974–984, Apr. 2010.
- [18] F. Ferranti, G. Antonini, T. Dhaene, L. Knockaert, and A. E. Ruehli, "Physics-based passivity-preserving parameterized model order reduction for PEEC circuit analysis," *IEEE Trans. Compon., Packag., Manuf. Technol.*, vol. 1, no. 3, pp. 399–409, Mar. 2011.
- [19] R. W. Freund, "Model reduction methods based on Krylov subspaces," *Acta Numer.*, vol. 12, pp. 267–319, Jul. 2013.
- [20] R. W. Freund, "The SPRIM algorithm for structure-preserving order reduction of general RCL circuits," in *Model Reduction for Circuit Simulation*. Dordrecht, The Netherlands: Springer, 2011, pp. 25–52.
- [21] Y. Su, F. Yang, and X. Zeng, "AMOR: An efficient aggregating based model order reduction method for many-terminal interconnect circuits," in *Proc. Design Autom. Conf.*, San Francisco, CA, USA, 2012, pp. 295–300.
- [22] C. S. Amin, M. H. Chowdhury, and Y. I. Ismail, "Realizable reduction of interconnect circuits including self and mutual inductances," *IEEE Trans. Comput.-Aided Des. Integr. Circuits Syst.*, vol. 24, no. 2, pp. 271–275, Feb. 2005.
- [23] Z. Ye, D. Vasilyev, Z. Zhu, and J. R. Phillips, "Sparse implicit projection (SIP) for reduction of general many-terminal networks," *Design Autom. Conf.*, San Francisco, CA, USA, 2008, pp. 1–2.
- [24] R. N. Shorten, P. Curran, K. Wulff, and E. Zeheb, "A note on spectral conditions for positive realness of transfer function matrices," *IEEE Trans. Autom. Control*, vol. 53, no. 5, pp. 1258–1261, Jun. 2008.
- [25] S. Boyd, V. Balakrishnan, and P. Kabamba, "A bisection method for computing the  $H_\infty$  norm of a transfer matrix and related problems," *Math. Control Signals Syst.*, vol. 2, no. 1, pp. 207–219, Jan. 1989.
- [26] S. Grivet-Talocia, "Passivity enforcement via perturbation of Hamiltonian matrices," *IEEE Trans. Circuits Syst. I, Reg. Papers*, vol. 51, no. 9, pp. 1755–1769, Sep. 2004.
- [27] Z. Bai and R. W. Freund, "Eigenvalue-based characterization and test for positive realness of scalar transfer functions," *IEEE Trans. Autom. Control*, vol. 45, no. 12, pp. 2396–2402, Dec. 2000.
- [28] C. Schroeder and T. Stykel, *Passivity Check in Passivation of LTI Systems*, document TR-368-2007, 2007.
- [29] B. Gustavsen and A. Semlyen, "Enforcing passivity for admittance matrices approximated by rational functions," *IEEE Trans. Power Syst.*, vol. 16, no. 1, pp. 97–104, Feb. 2001.
- [30] W. D. C. Boaventura, A. Semlyen, M. R. Iravani, and A. Lopes, "Sparse network equivalent based on time-domain fitting," *IEEE Trans. Power Del.*, vol. 17, no. 1, pp. 182–189, Jan. 2002.
- [31] C. K. Alexander and M. N. O. Sadiku, "Magnetically coupled circuits," in *Fundamentals of Electric Circuits*, New York, NY, USA: McGraw-Hill, 2007, pp. 564–566.
- [32] G. H. Golub and C. F. van Loan, "Positive definite system," in *Matrix Computation*, 4th ed. Baltimore, MD, USA: The Johns Hopkins Univ. Press, 2013, p. 160.
- [33] N. J. Higham, "Computing the nearest correlation matrix—A problem from finance," *IMA J. Numer. Anal.*, vol. 22, no. 3, pp. 329–343, 2002.
- [34] S. H. Cheng and N. J. Higham, "A modified Cholesky algorithm based on a symmetric indefinite factorization," *SIAM J. Matrix Anal. Appl.*, vol. 19, no. 4, pp. 1097–1110, Oct. 1998.
- [35] N. J. Higham, "Computing a nearest symmetric positive semidefinite matrix," *Linear Algebra Appl.*, vol. 103, pp. 103–118, May 1988.

- [36] J. D. Owens, M. Houston, D. Luebke, S. Green, J. E. Stone, and J. C. Phillips, "GPU computing," *Proc. IEEE*, vol. 96, no. 5, pp. 879–899, May 2008.
- [37] Y. Dou and K.-L. Wu, "Acceleration of physically derived micro-modeling circuit for packaging problems using graphics processing units," in *IEEE MTT-S Int. Microw. Symp. Dig.*, Jun. 2017, pp. 1638–1640.
- [38] Y. Dou and K.-L. Wu, "Acceleration of parallel computation for derived micro-modeling circuit by exploiting GPU memory bandwidth limit," in *Proc. IEEE Int. Conf. NEMO*, Seville, Spain, May 2017, pp. 146–148.



**Yuhang Dou** (S'13) received the B.S. degree in electronic engineering from the Nanjing University of Science and Technology, Nanjing, China, in 2012. She is currently pursuing the Ph.D. degree at the Chinese University of Hong Kong, Hong Kong.

Her current research interests include partial element equivalent circuit, full-wave circuit domain modeling for signal integrity and electromagnetic compatibility problems, and physics-based model-order reduction of PEEC model for electromagnetic problems in both the frequency and time domains.



**Ke-Li Wu** (M'90–SM'96–F'11) received the B.S. and M.Eng. degrees from the Nanjing University of Science and Technology, Nanjing, China, in 1982 and 1985, respectively, and the Ph.D. degree from Laval University, Quebec, QC, Canada, in 1989.

From 1989 to 1993, he was with the Communications Research Laboratory, McMaster University, Hamilton, ON, USA, as a Research Engineer and a Group Manager. In 1993, he joined the Corporate Research and Development Division, COM DEV International, as the largest Canadian space equipment manufacturer, where he was also a Principal Member of Technical Staff. Since 1999, he has been with the Chinese University of Hong Kong, Hong Kong, where he is a Professor and Director of the Radio Frequency Radiation Research Laboratory. He has authored or co-authored numerous publications in the areas of EM modeling and microwave passive components, and microwave filter and antenna engineering. His current research interests include EM-based circuit domain modeling of high-speed circuits, microwave passive circuits and systems, synthesis theory and practices of microwave filters, antennas for wireless terminals, LTCC-based multichip modules, and RF identification technologies.

Prof. Wu is a member of the IEEE MTT-8 Subcommittee (Filters and Passive Components) and also serves as a TPC member for many prestigious international conferences including International Microwave Symposium. He was an Associate Editor of the IEEE MTT-S IEEE TRANSACTIONS ON MICROWAVE THEORY TECHNOLOGY from 2006 to 2009. He was a recipient of the 1998 COM DEV Achievement Award for the development of exact EM design software of microwave filters and multiplexers and Asia-Pacific Microwave Conference Prize in 2008 and 2012.